nuclear fusion

PAPER • OPEN ACCESS

Global gyrokinetic simulations of magnetic geometry and radial electric field effects on turbulent transport in Wendelstein 7-X

To cite this article: A. Bañón Navarro *et al* 2026 *Nucl. Fusion* **66** 106021

View the article online for updates and enhancements.

You may also like

- Validation of hybrid-PIC simulations for advanced beam-driven FRC modeling
Roelof E. Groenewald, Scott Karbashewski, Sangeeta Gupta et al.

- On the transition to large fluxes and access to second stability in gyrokinetic simulations of electromagnetic turbulence in STEP
D. Kennedy, Y. Zhang, T. Adkins et al.

- Progress of understanding the effect of helium concentration on ion–electron collision and energy confinement on EAST
Qian Wang, Bin Zhang, Xianzu Gong et al.

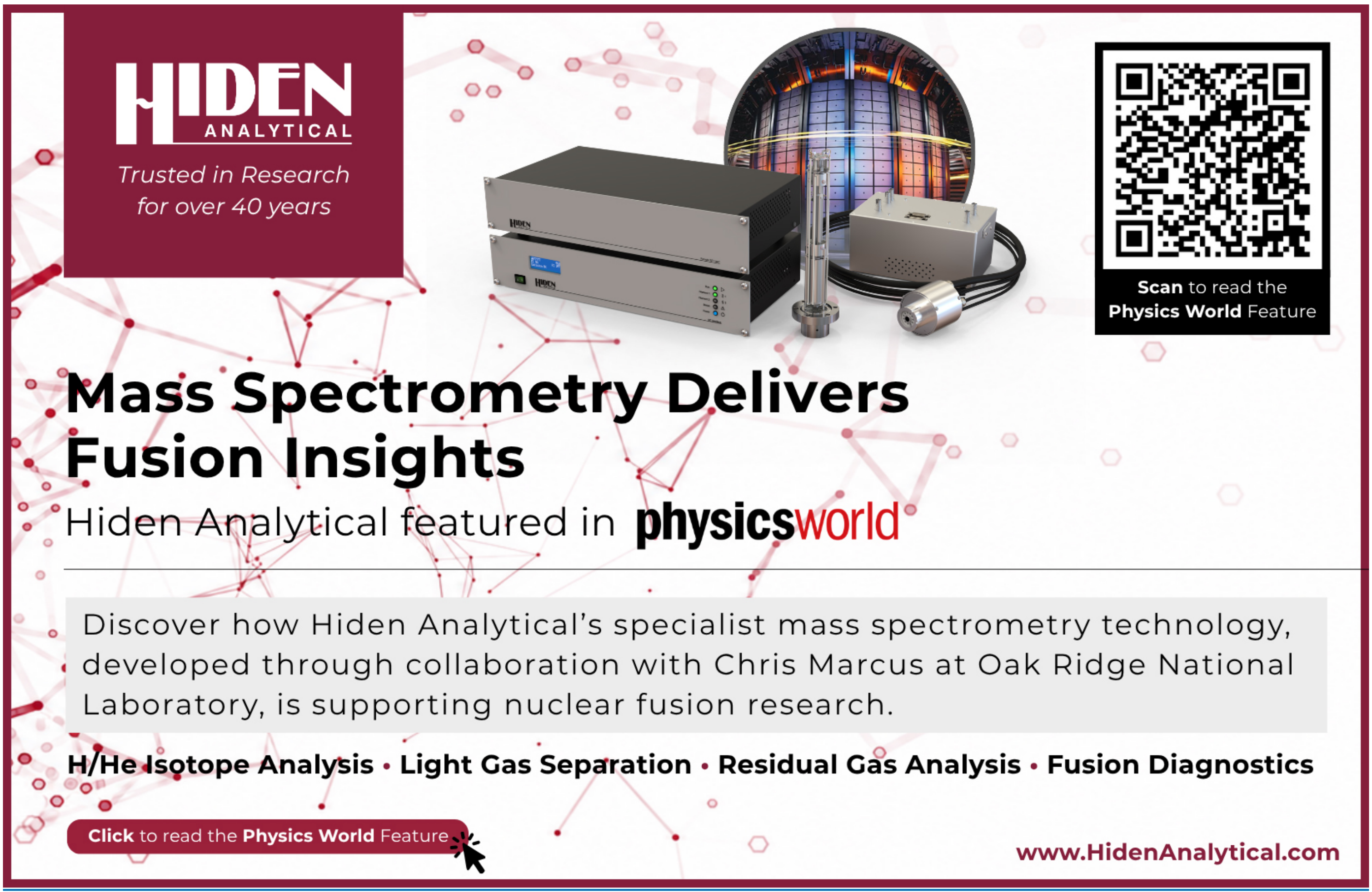

This content was downloaded from IP address 94.31.72.251 on 04/09/2026 at 07:22

OPEN ACCESS
IOP Publishing | International Atomic Energy Agency
Nuclear Fusion
Nucl. Fusion **66** (2026) 106021 (14pp)
https://doi.org/10.1088/1741-4326/ae9c53

Global gyrokinetic simulations of magnetic geometry and radial electric field effects on turbulent transport in Wendelstein 7-X

A. Bañón Navarro[1,*], L. Podavini[2], J.-P. Bähner[2], J. Smoniewski[3], S.K. Hansen[3,4], A. Di Siena[1], M. Porkolab[3], E.M. Edlund[5], A. von Stechow[2], S.A. Bozhenkov[2], O.P. Ford[2], G. Fuchert[2], A. Langenberg[2], N.A. Pablant[6], E. Pasch[2], P.Zs. Pölöskei[2], T. Romba[1], A. Zocco[2], O. Grulke[2,4], F. Jenko[1] and the W7-X Team[a]

[1] Max Planck Institute for Plasma Physics, Boltzmannstr. 2, 85748 Garching, Germany
[2] Max Planck Institute for Plasma Physics, Wendelsteinstr. 1, 17491 Greifswald, Germany
[3] MIT Plasma Science and Fusion Center, Cambridge, MA 02139, United States of America
[4] Technical University of Denmark, 2800 Kongens Lyngby, Denmark
[5] SUNY Cortland, Cortland, NY 13045, United States of America
[6] Princeton Plasma Physics Laboratory, Princeton, NJ 08540, United States of America

E-mail: alejandro.banon.navarro@ipp.mpg.de

Received 16 June 2026, revised 30 July 2026
Accepted for publication 20 August 2026
Published 2 September 2026

Abstract
We present a more detailed numerical analysis of the global GENE-3D simulations of Bähner *et al* (the W7-X Team) 2026 *Nucl. Fusion* **66** 016007, focusing on turbulent heat and particle transport and the role of the equilibrium radial electric field across mirror ratio and rotational transform (ι) configuration scans in Wendelstein 7-X (W7-X). Ion and electron heat fluxes show only mild sensitivity to both configuration parameters. The particle flux, however, exhibits a pronounced dependence on the mirror ratio, with the low-mirror configuration driving a strong inward particle pinch and the high-mirror configuration producing a net outward flux. Density fluctuation levels at fixed plasma profiles do not reproduce the experimentally observed configuration dependence in the mirror scan, a discrepancy that can be understood in terms of the simulations not satisfying power balance. A synthetic phase contrast imaging (PCI) diagnostic applied to the simulations reproduces the experimental ordering of the wavenumber and frequency spectra in the ι scan but not in the mirror scan, consistent with the same interpretation. The equilibrium radial electric field modifies turbulent transport, with the largest effect on the electron heat flux in regions of strong $E \times B$ shear. A controlled parametric study,

[a] See Grulke *et al* 2024 (https://doi.org/10.1088/1741-4326/ad2f4d) for the W7-X Team.
[*] Author to whom any correspondence should be addressed.

Original content from this work may be used under the terms of the Creative Commons Attribution 4.0 licence. Any further distribution of this work must maintain attribution to the author(s) and the title of the work, journal citation and DOI.

in which the E_r profile is systematically varied in amplitude and radial location, confirms that transport suppression follows the classical shear decorrelation criterion, being strongest where the shear rate exceeds the linear growth rate over the widest radial extent.

Keywords: stellarator, turbulence, transport, gyrokinetics, Wendelstein 7-X

(Some figures may appear in colour only in the online journal)

1. Introduction

Stellarators offer inherently steady-state operation and are free from the current-driven disruptions that constrain tokamak performance, but their non-axisymmetric geometry gives rise to strong neoclassical transport that must be reduced through careful magnetic field optimization. The Wendelstein 7-X (W7-X) stellarator has been specifically designed with this goal [1, 2], and recent experiments have confirmed this reduction and demonstrated sustained high-performance operation that would not have been attainable without this neoclassical optimization [3]. With neoclassical losses increasingly under control, turbulent transport has emerged as the dominant confinement limitation in W7-X [3, 4], making it a key target for turbulence optimization in future stellarator designs [5–7].

A distinctive feature of W7-X is its flexible magnetic configuration: the rotational transform, $\iota = \mathrm{d}\Psi_{\mathrm{pol}}/\mathrm{d}\Psi_{\mathrm{tor}}$, with Ψ_{pol} and Ψ_{tor} the poloidal and toroidal magnetic fluxes, and the magnetic mirror ratio, $r_{\mathrm{mir}} = [B_0(0) - B_0(\pi/5)]/[B_0(0) + B_0(\pi/5)]$, with B_0 the magnetic field strength on the magnetic axis evaluated at the toroidal angles $\phi = 0$ and $\phi = \pi/5$, i.e. at the corner and center of a field period [8], can be varied experimentally, enabling controlled scans of magnetic geometry [9] and providing a unique opportunity to investigate how geometric variations influence turbulent transport [10–12]. The configurations considered here span mirror ratios of -0.7% (low mirror), 3.8% (standard), and 9.7% (high mirror) [8]. In [8], this was explored through phase contrast imaging measurements of density fluctuations across mirror ratio and ι scans, complemented by flux-tube and global gyrokinetic simulations. Increasing ι was found to reduce fluctuation amplitudes, a trend reproduced by simulations and attributed to enhanced finite Larmor radius and local magnetic shear effects [12]. In contrast, increasing the mirror ratio enhanced fluctuation levels experimentally, a trend not reproduced at fixed plasma profiles.

Here, we present a more detailed analysis of the global GENE-3D [13, 14] simulations presented in [8], focusing in particular on the turbulent transport channels—ion and electron heat fluxes and particle fluxes—as well as the effect of the equilibrium radial electric field and its associated $E \times B$ shear, which were not systematically addressed there. Since E_r is set by the neoclassical ambipolarity constraint [2, 15, 16], it varies between configurations alongside the magnetic geometry. The radial shear of the associated $E \times B$ flow can suppress turbulence through shear decorrelation [17–19], and how effective this suppression is depends on the growth rate of the dominant instabilities and the radial extent over which the shear exceeds it, both of which also change with configuration. To enable a direct comparison with the line-integrated phase contrast imaging (PCI) measurements of [8], the simulations are also post-processed with the synthetic PCI diagnostic [20] developed for W7-X.

The paper is organized as follows. Section 2 summarizes the experimental discharges and configuration scans. Section 3 describes the numerical setup. Sections 4 and 5 present results on magnetic configuration and radial electric field effects, respectively. Conclusions are given in section 6.

2. Experimental discharge and configuration scan

The simulations presented here are based on experimentally realized discharges from configuration scans performed during the W7-X operation phase OP2.1 (autumn 2022 – spring 2023), in which the rotational transform and mirror ratio were systematically varied while maintaining comparable density and temperature profiles; we refer the reader to [8] for a detailed description of the experimental setup and measurements.

The reference experiments employed electron cyclotron resonance heating (ECRH) with gas fueling, which is the standard scenario for long-pulse W7-X operation [1, 3]. This scenario produces relatively flat density profiles in the inner plasma core, peaked electron temperature profiles, and clamped ion temperature profiles with $T_{\mathrm{i}} < T_{\mathrm{e}}$. Core electron densities are in the range $n_{\mathrm{e}} \sim 3\text{–}4 \times 10^{19}\,\mathrm{m}^{-3}$ with central electron temperatures of order 4–6 keV.

The radial profiles of ion temperature, electron temperature, and density used in the simulations are shown in figure 1. They correspond to the model profiles of [8], fitted to the experimental measurements. The same profiles are used for all configurations within each scan, so that differences in the simulated transport can be attributed to the magnetic geometry alone.

The corresponding equilibrium radial electric field profiles are displayed in figure 2. In all configurations, E_r is positive in the inner core (the electron root expected for central ECRH), changes sign around $\rho_{\mathrm{tor}} \sim 0.2\text{–}0.3$, and becomes negative across the outer region with amplitudes of order -5 to $-8\ \mathrm{kV\,m^{-1}}$ (deepest near $\rho_{\mathrm{tor}} \sim 0.7$), consistent with the neoclassical ambipolar radial electric field in ECRH W7-X plasmas [15]. The E_r profiles are taken from the neoclassical ambipolarity calculation of [8], performed with the NEOTRANSP code [21], in which the electron-to-ion root transition is treated as a simple switch: the electron root is selected in the inner core and the ion root in the outer region. These profiles are used as a prescribed background field in all simulations.

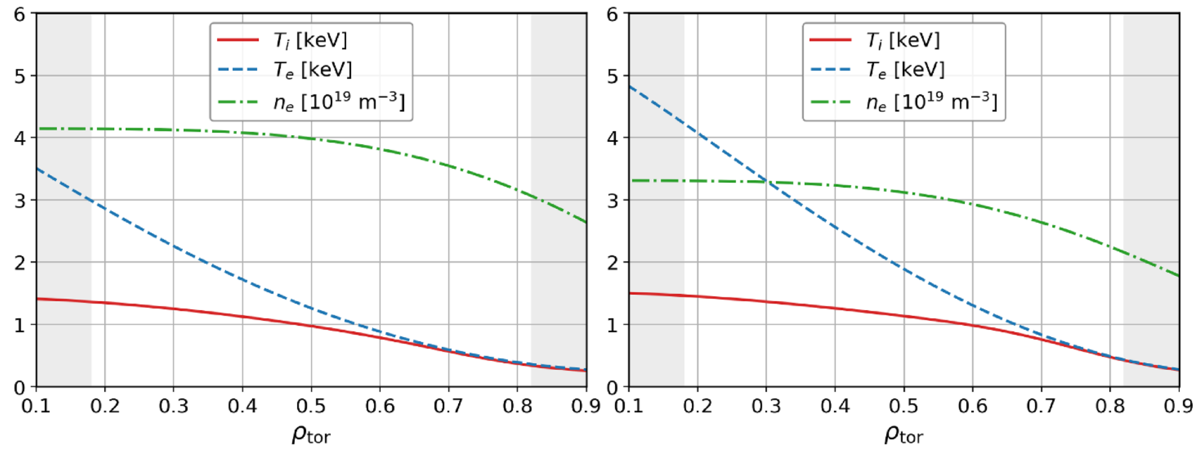

Figure 1. Radial profiles used in the simulations. *Left*: profiles for the mirror scan configurations. *Right*: profiles for the ι scan configurations. Ion temperature T_i is shown in red (keV), electron temperature T_e in dashed blue (keV), and electron density n_e in green dash-dotted lines ($10^{19}\,\mathrm{m}^{-3}$). Grey shaded areas mark the buffer zones of the global simulations.

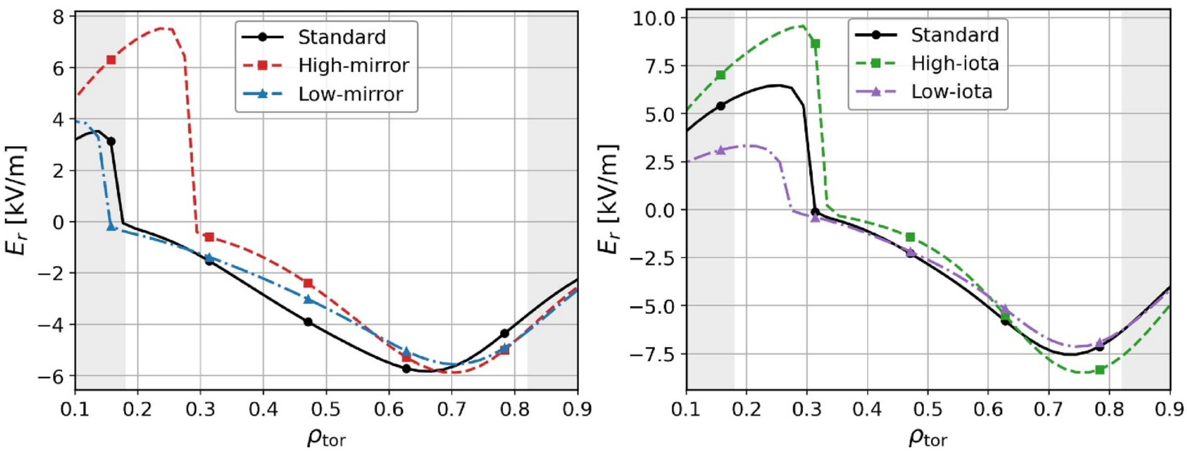

Figure 2. Radial electric field profiles E_r (kV m^{-1}) used in the simulations. *Left*: mirror scan configurations with standard (black solid), high-mirror (red dashed), and low-mirror (blue dash-dotted). *Right*: ι scan configurations with standard (black solid), high-ι (green dashed), and low-ι (purple dash-dotted). Grey shaded areas mark the buffer zones of the global simulations.

3. Global gyrokinetic modeling

The simulations were performed with the global gyrokinetic turbulence code GENE-3D, an extension of the Eulerian gyrokinetic code GENE [22] to fully three-dimensional stellarator geometries [13, 14]. The original GENE framework employs a field-aligned coordinate system [23] and a δf formulation [24], supporting electromagnetic, multispecies, and collisional simulations [25]. GENE-3D retains these capabilities while enabling the treatment of realistic non-axisymmetric magnetic equilibria. Fully three-dimensional geometry is incorporated via an interface to the MHD equilibrium code GVEC [26], which provides the magnetic equilibrium, including metric elements, curvature, magnetic shear, and other geometric quantities required by the gyrokinetic model.

The nonlinear electromagnetic gyrokinetic Vlasov–Maxwell system is solved in five-dimensional phase space. Simulations were carried out with kinetic electrons using the physical mass ratio, including electromagnetic fluctuations and collisional effects via a linearized collision operator. The radial domain considered in this work spans $x = \rho_{tor} \in [0.1, 0.9]$, with numerical resolution $(x, y, z, v_\parallel, \mu) = (300, 256, 63, 64, 16)$. Here, $\rho_{tor} = \sqrt{\Phi_{tor}/\Phi_{edge}}$, where Φ_{tor} is the toroidal flux and Φ_{edge} its value at the last closed flux surface. The remaining phase-space coordinates are defined as follows: y denotes the binormal direction, z the field-aligned coordinate, $v_\parallel$ the parallel velocity, and μ the magnetic moment. This resolution is that of the global GENE-3D simulations of [8]. Convergence in the parallel resolution was verified for the mirror configurations: nonlinear simulations with $n_z = 126$ yield heat fluxes consistent with those at $n_z = 63$. The lower resolution was therefore adopted for the production runs, given the computational cost of these global electromagnetic simulations with kinetic electrons at the physical mass ratio. The minimum toroidal mode number resolved in the simulations is $n_0 = 5$, consistent with the field periodicity of W7-X, such that one field period (1/5 of the flux surface) is simulated. The velocity-space domain extends to $v_\parallel = \pm 3.45\,c_s$ and $\mu_{max} = 11.9\,T_{s,0}/B_0$, where $T_{s,0}$ is the temperature of species s at the reference position $x_0 = 0.5$, and B_0

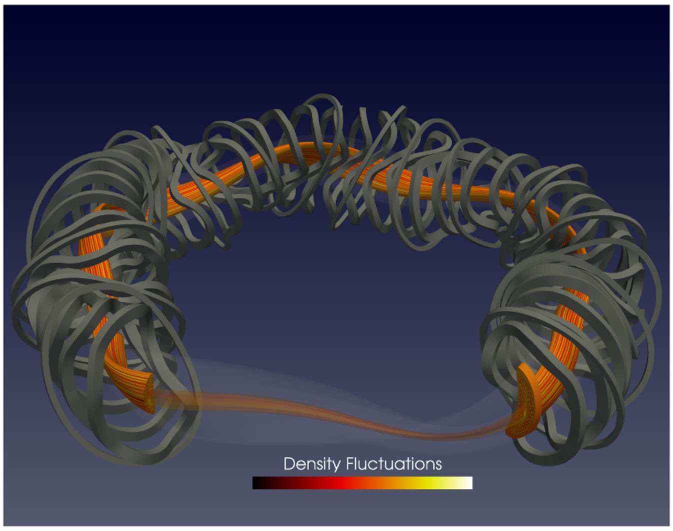

Figure 3. Density fluctuations from a radially global GENE-3D simulation in a W7-X configuration, illustrating the three-dimensional character of the turbulence.

is the on-axis magnetic field strength. Here, $c_s = \sqrt{T_{\mathrm{e},0}/m_\mathrm{i}}$ is the sound speed, where $T_{\mathrm{e},0}$ is the electron temperature at the reference position and m_i is the ion mass.

The simulations employ zero Dirichlet boundary conditions in the radial direction. The simulations are performed in gradient-driven mode, in which a Krook-type heat and particle source maintains the plasma profiles close to their initial values, so that the turbulence drive remains stationary throughout the simulation. To avoid numerical instabilities near the boundaries, buffer zones covering 10% of the radial domain are applied on each side, where a Krook damping operator is used [25] with a coefficient of $10\,c_s/a$, significantly larger than the expected linear growth rates. In addition, the Krook-type heat and particle source [25] has a relaxation rate of $0.02\,c_s/a$, such that the temperature and density profiles evolve on time scales longer than those of the linear phase. Finally, to assess the influence of the equilibrium radial electric field and its associated $E \times B$ shear, simulations were performed both with and without the neoclassically calculated radial electric field.

Throughout this paper, $Q_s \cdot A$ denotes the species-s heat flux times the flux-surface area A—a heat flow, in MW—while the reduced-domain analysis of section 5 reports the electrostatic fluxes in gyro-Bohm units; the electromagnetic contribution to the transport is small for these cases. All flux profiles are averaged over the quasi-stationary phase of each simulation, with averaging windows of up to $\sim 100\,a/c_s$ for the full-domain simulations and substantially longer over the saturated state for the computationally cheaper reduced-domain simulations of section 5; shaded bands in the flux figures indicate one standard deviation of the temporal variation over this window, and grey shaded areas in the radial-profile figures mark the buffer zones.

An example of the simulated density fluctuation structure is shown in figure 3, illustrating the three-dimensional character of W7-X turbulence.

4. Impact of magnetic configuration on turbulence and transport

We investigate the effect of two configuration parameters—the magnetic mirror ratio and the rotational transform (ι) — on turbulent transport in W7-X. For each parameter, radial profiles of ion and electron heat fluxes, particle fluxes, and density fluctuations are evaluated with the equilibrium E_r profiles of figure 2 imposed as a background field. Results from the mirror scan are presented first, followed by the ι scan.

4.1. Effect of magnetic mirror ratio

The ion heat flux exhibits a pronounced peak around $\rho_{\mathrm{tor}} = 0.65$, reaching 6–7 MW, as shown in figure 4 (top). This substantially exceeds even the total injected ECRH power in the reference discharges [8], and far exceeds the fraction of it transferred to the ions by collisional equipartition, indicating that the resulting fluxes do not satisfy power balance, since the underlying profiles are fixed and not evolved self-consistently. Turbulence and transport are highly sensitive to profile shapes, particularly to the gradients, due to the stiffness of the system [27]. Nevertheless, even in the absence of power balance, the relative differences induced by magnetic geometry provide insight into turbulence behavior. The variations are mild: the low-mirror configuration exhibits the highest fluxes, most pronounced in the inner half.

Variations are also mild for the electron heat flux (figure 4, middle), though with opposite ordering. The fluxes are more uniform and less peaked, with values around 3–4 MW, comparable to the total injected ECRH power [8]. This broader radial profile is consistent with the wider extent over which the electron channel is driven: the normalized inverse temperature gradient scale length $a/L_{T,\mathrm{e}}$, with $L_T = -T/(\mathrm{d}T/\mathrm{d}r)$ and a the minor radius, is already significant in the inner half of

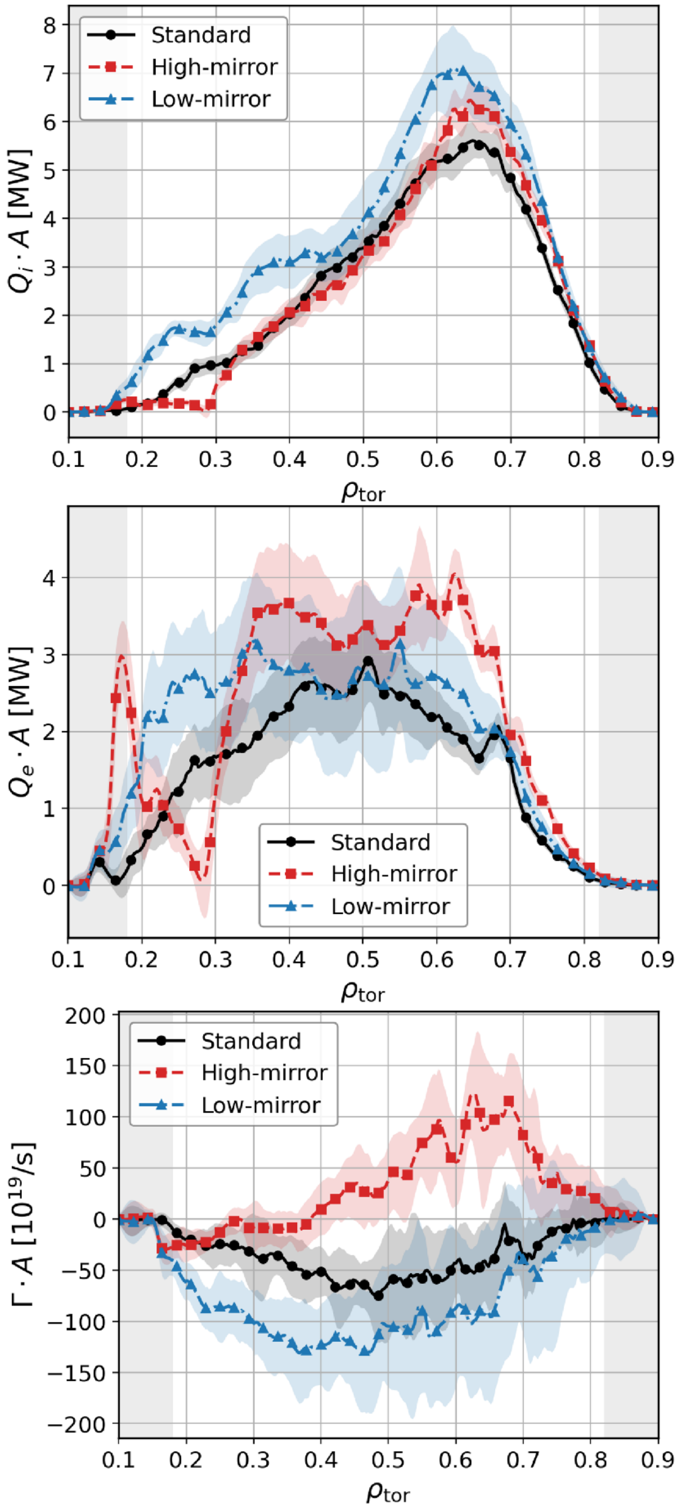

Figure 4. Radial profiles of the ion heat flux Q_i (*top*), electron heat flux Q_e (*middle*), and particle flux Γ (*bottom*) for the three mirror scan configurations: standard (black solid), high-mirror (red dashed), and low-mirror (blue dash-dotted).

the plasma due to the strongly peaked T_e from on-axis ECRH (figure 1), whereas $a/L_{T,\mathrm{i}}$ remains small inside $\rho_\mathrm{tor} \simeq 0.4$ and only becomes large in the outer region where Q_i peaks. Q_e is systematically higher in the high-mirror configuration than in the standard and low-mirror cases across the mid-radius region ($\rho_\mathrm{tor} \simeq 0.35$–$0.65$); in the deep core near $\rho_\mathrm{tor} \simeq 0.25$, where its E_r shear is strongest, Q_e is instead locally suppressed, an effect examined in section 5.

In contrast, the particle flux shows a more pronounced dependence on the mirror ratio (figure 4, bottom). The low-mirror configuration exhibits a strong inward flux (negative Γ), indicative of a significant density pinch. The standard

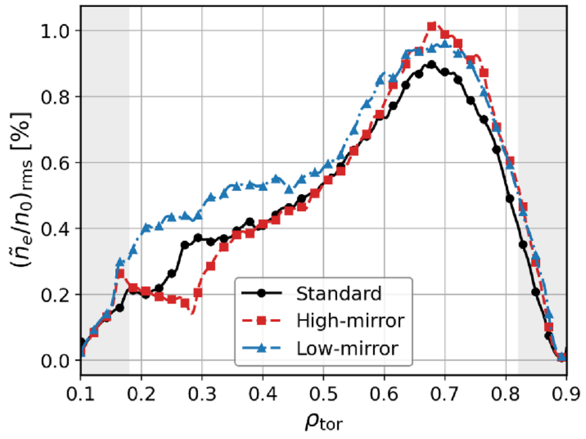

Figure 5. Radial profiles of root-mean-square electron density fluctuations for the mirror scan configurations: standard (black solid), high-mirror (red dashed), and low-mirror (blue dash-dotted). Overall, the fluctuation amplitudes are similar across the three configurations.

configuration also shows an inward flux, though weaker, while the high-mirror configuration displays a net outward flux over a broad radial range, consistent with the absence of a net inward pinch. These results agree with previous studies [28], which show that the pinch is driven by passing electrons, whose effect is enhanced in low-mirror configurations. Note that these particle fluxes are not consistent with particle balance: the stationary net particle flux in these ECRH discharges without core fueling is essentially zero, and at fixed gradients even a small deviation of the prescribed density profile from the zero-flux condition drives turbulent particle fluxes of gyro-Bohm magnitude.

Interestingly, differences in particle flux do not directly translate into differences in the root-mean-square (RMS) density fluctuations across the mirror configurations (figure 5). This is because the particle flux depends not only on the amplitudes of the density and potential fluctuations but also on their cross-phase. Overall, the RMS density fluctuations show comparable peak amplitudes across the mirror configurations, with the low-mirror case marginally larger in the inner half. This contrasts with PCI measurements [8], which indicate larger fluctuations in the high-mirror configuration compared to the low-mirror case, a trend not reproduced by the simulations at fixed profiles.

The turbulent $E \times B$ velocity, which together with the density fluctuations sets the particle flux, supports this interpretation. Figure 6 shows its RMS, computed as $(\partial\tilde{\phi}/\partial y)/B$. The peak velocity amplitudes differ by 10%–20% between the mirror configurations, and the profiles remain close over most of the radial domain, apart from a localized reduction of the high-mirror amplitude around $\rho_{\rm tor} \simeq 0.3$, where $Q_{\rm e}$ is also locally suppressed. The particle fluxes instead differ in magnitude and sign (figure 4). Amplitude differences of this size cannot account for a sign reversal of the flux; the differences in particle flux therefore originate from the cross-phase rather than from the fluctuation amplitudes.

The observed discrepancy between simulations and PCI measurements in the mirror scan can be understood in terms of power balance. As explicitly noted in [8], geometry effects on turbulence alone are insufficient to explain the experimentally observed trend — both local and global gyrokinetic simulations at fixed profiles fail to reproduce it. Since the simulations are not in power balance, the particle and heat fluxes differ between configurations in a way that is inconsistent with the experiment. The strong inward particle pinch in the low-mirror configuration would, if the profiles were evolved self-consistently, cause the density to steepen, while the outward flux in the high-mirror configuration would instead flatten the density profile. The net effect on the turbulence cannot be anticipated from these tendencies alone: a steeper density gradient stabilizes ITG modes but destabilizes trapped-electron modes, and the balance between the two depends on the configuration. What the particle fluxes do show is that self-consistent profile evolution would act differently on each configuration, making it a candidate explanation for the experimental mirror trend that fixed-profile simulations do not reproduce. Such density-profile changes would also modify, through the ambipolarity condition, the neoclassical radial electric field and its $E \times B$ shear, so that the particle transport would feed back on the $E \times B$-shear stabilization examined in section 5. Since the experimentally measured profiles show only small differences between mirror configurations within diagnostic uncertainties [8], any self-consistent profile evolution must produce configuration-dependent changes that remain within these uncertainties while still reproducing the observed fluctuation trend. Evolving the profiles via TANGO [29–32] is therefore expected to modify the configuration-dependent trends, potentially bringing them closer to the experimental observations. This is supported by previous applications of the GENE–TANGO framework to other W7-X discharges [33, 34], where self-consistent profile evolution was shown to bring simulations into quantitative agreement with experiment.

The mirror ratio scan thus reveals a clear separation between transport channels: heat fluxes are only mildly sensitive to the configuration, while the particle transport shows a pronounced dependence.

4.2. Effect of rotational transform (ι)

We now turn to the effect of varying the rotational transform, keeping the mirror ratio fixed at the standard configuration value. Ion and electron heat fluxes are largely insensitive to variations in ι outside the deep core, with profiles nearly overlapping for $\rho_{\rm tor} \gtrsim 0.5$ (figure 7, top and middle). The ion flux peaks around $\rho_{\rm tor} \simeq 0.7$ with values around 4 MW, still exceeding the total injected ECRH power, indicating that these simulations are also not in power balance. Large electron-heat-flux overshoots appear in the deep core around $\rho_{\rm tor} \sim 0.2$–0.3, just outside the buffer zone, and are likely numerical artifacts of the boundary damping applied there [13, 25]. Particle fluxes show qualitatively similar shapes across configurations (figure 7, bottom), with inward flux in the inner half and outward flux

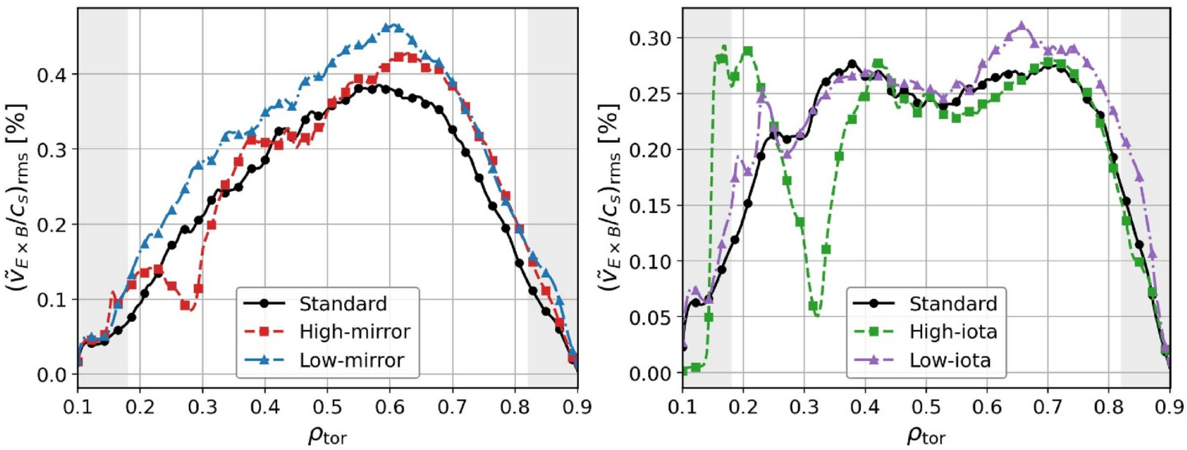

Figure 6. Radial profiles of the RMS turbulent radial $E\times B$ velocity, computed as $(\partial\tilde{\phi}/\partial y)/B$. *Left*: mirror scan configurations: standard (black solid), high-mirror (red dashed), and low-mirror (blue dash-dotted). *Right*: ι scan configurations: standard (black solid), high-ι (green dashed), and low-ι (purple dash-dotted).

toward the edge. The low-ι configuration exhibits a stronger inward flux than the standard and high-ι cases.

RMS electron density fluctuations are largely similar across the ι configurations (figure 8), with only minor differences in the core region ($\rho\sim 0.2$–0.5), where the low-ι case exhibits slightly larger fluctuations than the standard and high-ι configurations. This is consistent with PCI measurements reported in [8] and with theoretical expectations [12]. The turbulent $E\times B$ velocity amplitudes are also similar across the ι configurations (figure 6, right); the localized structure of the high-ι curve in the deep core ($\rho_{\rm tor}\simeq 0.2$–0.3) mirrors the electron-heat-flux overshoots in this region (figure 7, middle), which are likely numerical artifacts of the boundary damping. Since the PCI signal is line-integrated along the diagnostic line of sight rather than localized at a single radius, a direct comparison to the experimental spectra is performed in section 4.3 using a synthetic PCI diagnostic.

Overall, the ι scan shows small differences across all transport channels, in contrast to the mirror scan where particle transport exhibits a strong configuration dependence. The simulations already reproduce the PCI ordering at fixed profiles; given the overall transport similarity, self-consistent profile evolution is not expected to substantially alter this agreement.

4.3. Synthetic PCI comparison

To enable a direct comparison with the experimental measurements of [8], the simulated density fluctuations are post-processed with the synthetic PCI diagnostic developed for W7-X [20]. The synthetic diagnostic interpolates $\tilde{n}_{\rm e}(x_\perp,z)$ from the simulation onto the PCI lines of sight in PEST coordinates, computes the line-integrated phase shift $\tilde{\phi}=-r_{\rm e}\lambda_0\int_{\rm LoS}\tilde{n}_{\rm e}\,{\rm d}z$, where $r_{\rm e}$ is the classical electron radius and λ_0 the probing laser wavelength, and propagates it through the instrument response, including aperture diffraction, the phase-plate cutoff at $k_{\rm min}\simeq 1.6\,{\rm cm}^{-1}$, and integration over the detector elements. We refer the reader to [20] for a detailed description. The synthetic and experimental spectra are compared directly on the same absolute axes in figure 9, in units of squared density fluctuations per wavenumber and per frequency; the instrument response is accounted for in both. Despite the lack of power balance, the absolute amplitudes agree to within a factor of $\sim$3 over most of the spectral range, and the spectral slopes are broadly reproduced.

The synthetic PCI diagnostic is applied to the full simulation domain. Figure 9 (bottom row) shows the wavenumber and frequency spectra for the ι scan, with the experimental PCI spectra (solid) overlaid on the synthetic ones (dashed). A clear configuration ordering is visible in the synthetic spectra: the spectral power decreases monotonically from low to high ι across most of the resolved range, both in k and in f. This trend reproduces the experimental ordering, though the separation between configurations is larger in the synthetic spectra than in the measurements. Note that the synthetic PCI ordering is more pronounced than the radial RMS density-fluctuation profile of figure 8 would suggest. The two diagnostics are not directly comparable: the synthetic PCI is line-integrated along the diagnostic chords and band-limited by the phase-plate cutoff and instrument response, while figure 8 is an RMS averaged over the binormal, field-aligned, and time coordinates at each flux surface.

For the mirror scan, the synthetic PCI spectra are essentially identical across the three configurations, both in k and in f, while the experimental spectra split by a factor of $\sim$2–3 between the low- and high-mirror configurations (figure 9, top row). The experimental configuration ordering is therefore not reproduced. This reinforces the conclusion of section 4.1: at fixed plasma profiles, geometry effects on turbulence alone are insufficient to explain the experimental mirror dependence.

5. Effect of the equilibrium radial electric field

We now isolate the impact of the equilibrium radial electric field on turbulent transport. For each magnetic configuration, simulations without a background E_r are compared to

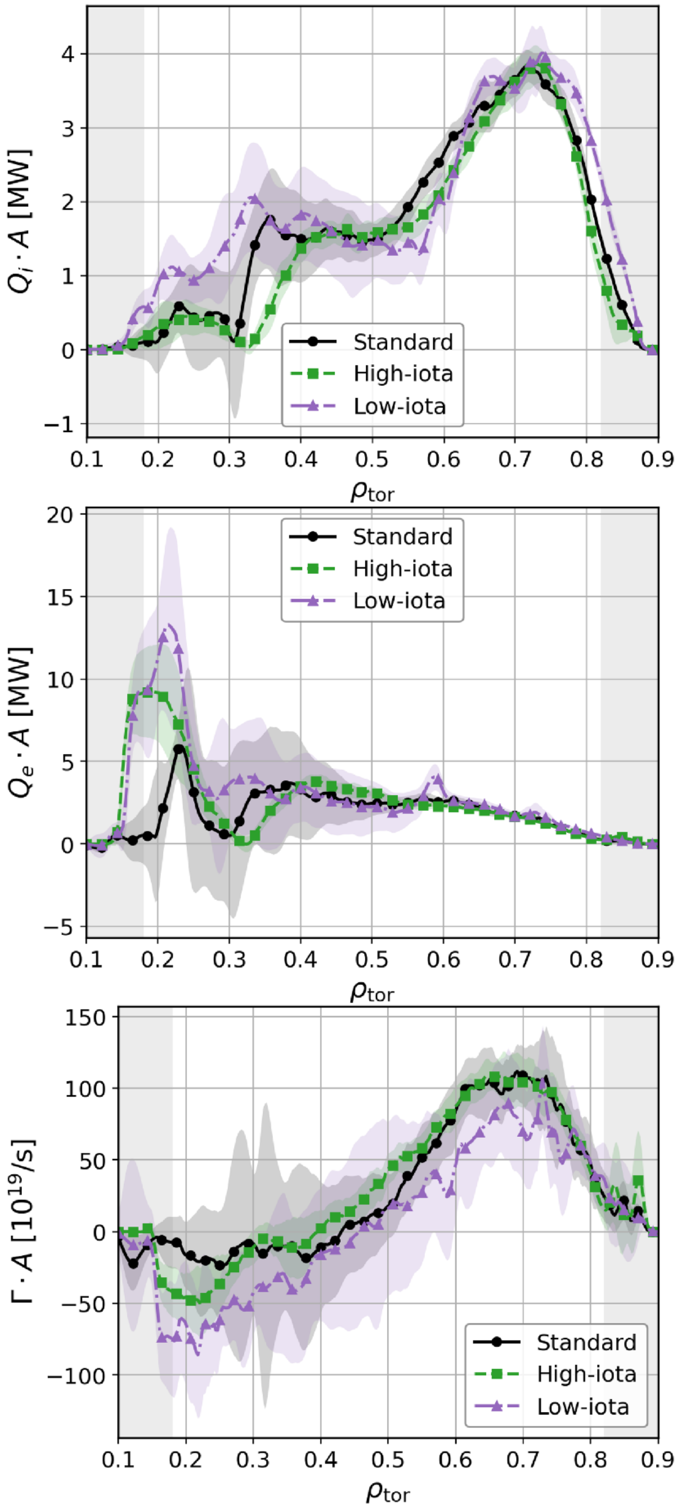

Figure 7. Radial profiles of ion heat flux $Q_{\rm i}$ (*top*), electron heat flux $Q_{\rm e}$ (*middle*), and particle flux Γ (*bottom*) for the ι scan configurations: standard (black solid), high-ι (green dashed), and low-ι (purple dash-dotted). Particle fluxes are similar across configurations, with inward flux inside $\rho \sim 0.4$ and outward flux outside.

simulations including the neoclassically calculated E_r profile shown in figure 2. Since E_r is set by neoclassical ambipolarity on the fixed density and temperature profiles, it inherits the same power-balance limitation: any turbulent profile modification would feed back into E_r and its shear. The present analysis therefore characterizes the turbulent response to a prescribed $E \times B$ shear, not the steady state of a coupled neoclassical–turbulent system.

We begin by considering a representative case to illustrate the effect of E_r on the heat fluxes. Figure 10 shows the ion and

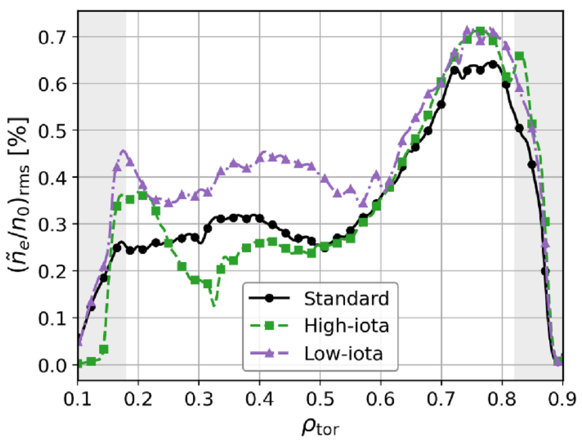

Figure 8. Radial profiles of root-mean-square electron density fluctuations for the ι scan configurations: standard (black solid), high-ι (green dashed), and low-ι (purple dash-dotted). Fluctuation amplitudes are generally similar across configurations, with small differences observed mainly in the inner half of the plasma.

electron heat fluxes for the high-mirror configuration, with and without the background radial electric field. Similar qualitative trends are observed for the other mirror and ι configurations (not shown).

Two main features can be identified. First, the ion heat flux peak around $\rho \sim 0.65$ is reduced in the presence of E_r. This region does not coincide with the strongest $E \times B$ shear, which peaks around $\rho \sim 0.3$ where the ion heat flux is already very low, suggesting that the reduction is attributable to the direct stabilizing effect of the background E_r rather than to its shear, as previously reported for stellarator plasmas [35, 36]. Second, for the electron heat flux, the largest differences are observed around $\rho \sim 0.25$–0.35, coinciding with the region of strongest $E \times B$ shear. The particle flux is only weakly affected: the differences between the simulations with and without E_r remain within the temporal variability (figure 10, right).

To better quantify these effects and relate them to the underlying $E \times B$ shear, we compute the percentage difference in the electron heat flux between simulations without and with equilibrium E_r as

$$\Delta Q_{\rm e}\,(\%) = \frac{Q_{\rm e,off} - Q_{\rm e,on}}{\max\left(|Q_{\rm e,off}|, |Q_{\rm e,on}|\right)} \times 100, \qquad (1)$$

where $Q_{\rm e,off}$ and $Q_{\rm e,on}$ denote the electron heat flux obtained without and with the equilibrium radial electric field, respectively. The normalization by the larger of the two fluxes bounds $\Delta Q_{\rm e}$ to $[-100\%, +100\%]$. Positive values indicate transport suppression, while negative values indicate destabilization. Figure 11 shows $\Delta Q_{\rm e}$ together with the corresponding equilibrium $E \times B$ shear rate $\omega_{E\times B}$, defined as

$$\omega_{E\times B} = \rho_{\rm tor} \frac{\partial}{\partial \rho_{\rm tor}} \left(\frac{E_r}{\rho_{\rm tor} \langle B \rangle_{\rm FS}} \right), \qquad (2)$$

where $\langle B \rangle_{\rm FS}$ denotes the full-surface average of the magnetic field, for both mirror and ι scans. The largest positive values of $\Delta Q_{\rm e}$ (strongest suppression) are found in regions of significant equilibrium $E \times B$ shear, confirming a clear radial correlation between transport reduction and the shear rate. A more moderate but non-negligible suppression is also observed in the region $\rho \sim 0.4$–0.7, where $E \times B$ shear is weaker but the background E_r remains substantial, consistent with the direct stabilizing effect of E_r [35, 36]. The destabilization observed near $\rho \sim 0.2$ sits just outside the inner core buffer zone and is a numerical artifact of the boundary damping [13, 25].

To better isolate the role of $E \times B$ shear and understand the conditions under which it effectively suppresses transport, we now turn to a controlled parametric study.

5.1. Setup of the parametric $E \times B$ shear study

In the previous section, we observed that the strongest $E \times B$ shear occurs around $\rho \sim 0.3$, where the ion heat flux is already very low even in the absence of the imposed shear. This makes it difficult to isolate the direct impact of shear on turbulent transport.

To better isolate the role of $E \times B$ shear, we perform a series of controlled numerical experiments using reduced radial domains. Three simulations are carried out, each centered at a different radial location ($\rho = 0.25$, 0.45, and 0.65), with a radial domain width of $\Delta\rho = 0.3$. The reduced-domain simulations use the standard configuration and the same equilibrium profiles as in figure 1; only the imposed radial electric field differs, as described below. In each case, an equilibrium radial electric field is imposed such that the peak of the $E \times B$ shear is centered at the chosen radial position. By shifting the location of the imposed shear, we probe regions with different levels of turbulent transport, since the turbulent heat flux increases from the inner core toward the outer core.

The radial electric field profile is constructed using the equilibrium E_r from the high-mirror configuration as a reference (which exhibits the strongest shear among the configurations considered, see figure 2), and then applied to simulations of the standard-mirror configuration, which provides a cleaner baseline unaffected by the strongest shear. In addition to the nominal shear amplitude, two additional cases are considered where the E_r profile is scaled by approximately a factor of two and four, resulting in increased shear amplitudes, allowing us to systematically investigate the response of the turbulence to stronger $E \times B$ shear. We emphasize that this scan is intended as a controlled probe of the shear-decorrelation criterion rather than an experimentally accessible scenario. The nominal E_r profile already produces an $E \times B$ shear that exceeds typical mid-radius values in high-performance W7-X discharges; the $\sim 2\times$ and $\sim 4\times$ amplifications therefore lie well beyond the experimentally realized range. The nominal E_r profile is used here only as a physically motivated building block whose amplitude is varied to systematically probe shear decorrelation.

Figure 12 shows the imposed radial electric field (left) and the corresponding $E \times B$ shear rate $\omega_{E\times B}$ (right), as defined in equation (2), for the simulation centered at $\rho = 0.45$. The

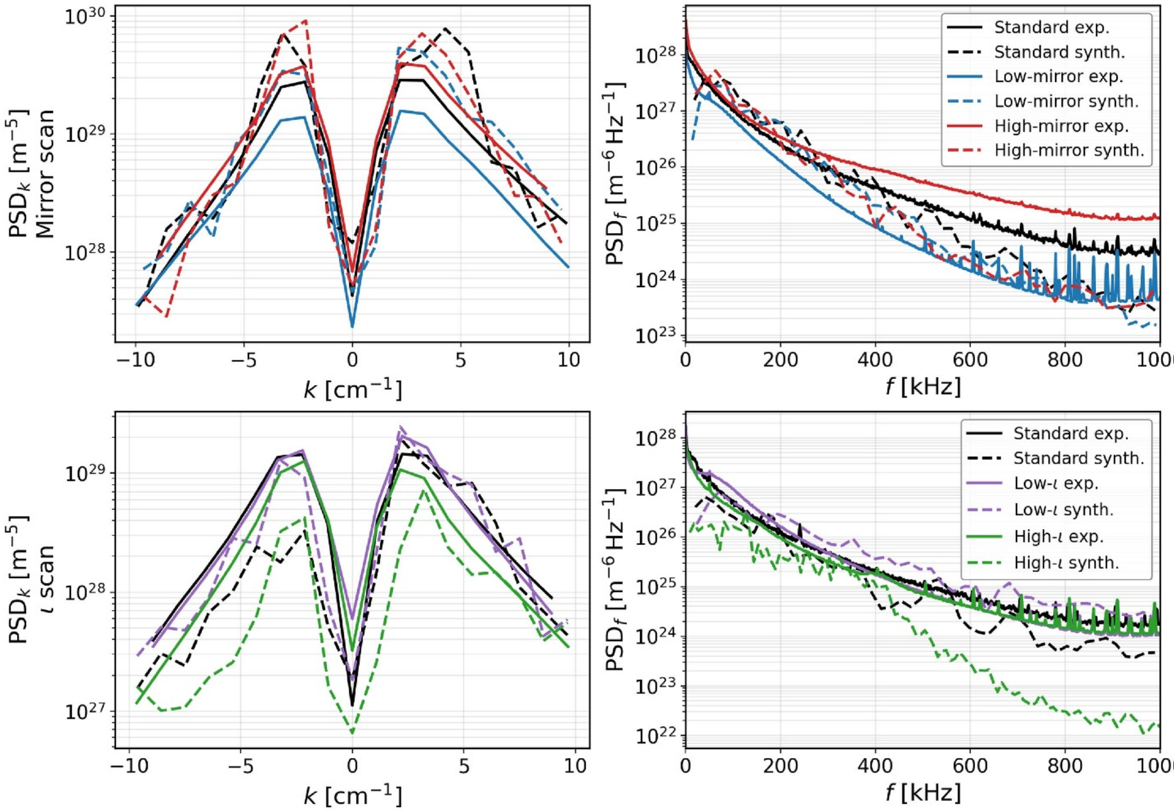

Figure 9. Wavenumber (*left column*) and frequency (*right column*) spectra of the density fluctuations from the experimental PCI (solid) and the synthetic PCI applied to the simulations (dashed), on the same absolute axes. *Top row*: mirror scan: standard (black), low-mirror (blue), and high-mirror (red). *Bottom row*: ι scan: standard (black), low-ι (purple), and high-ι (green). Experimental data from the discharges of [8].

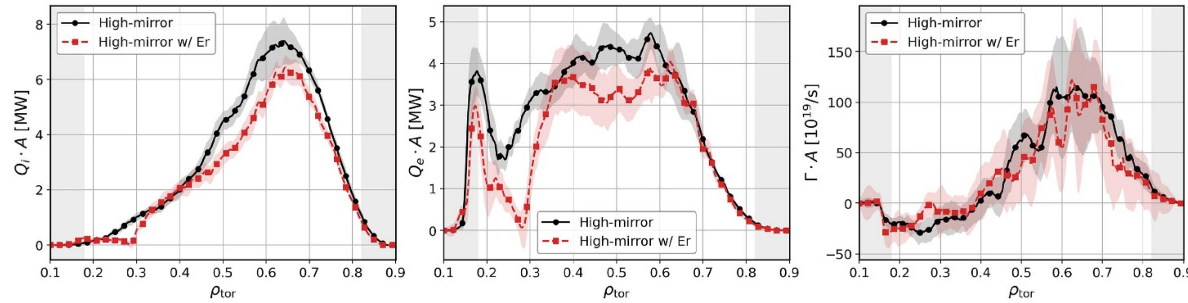

Figure 10. Ion heat flux Q_i (*left*), electron heat flux Q_e (*center*), and particle flux Γ (*right*) for the high-mirror configuration. Black solid lines: without E_r; red dashed lines: with equilibrium radial electric field.

three curves correspond to the nominal E_r profile and two cases where it is scaled by approximately a factor of two and four. The resulting shear amplitudes increase accordingly, though not by exactly those factors. The horizontal line in the right panel indicates the maximum linear growth rate $\gamma = 0.08\,c_s/a$ for the domain centered at $\rho = 0.45$, obtained from a linear global simulation without a background radial electric field. Radial regions where $\omega_{E\times B} > \gamma$ are expected to be stabilized by shear decorrelation.

We begin by comparing the heat fluxes in the full radial domain with those obtained from the reduced domains. Figure 13 shows the ion heat flux, electron heat flux, and electron particle flux for the standard configuration, comparing the full-domain results with the reduced-domain simulations centered at $\rho = 0.25$, 0.45, and 0.65, all performed without an imposed background E_r.

While boundary effects lower the fluxes in the reduced domains centered at $\rho = 0.25$ and 0.45 and raise the peak at $\rho = 0.65$, the qualitative radial trend of increasing heat flux from the inner core toward the outer core is well reproduced in all cases. We note, however, that the full-domain electron heat flux exhibits a local modulation near $\rho \sim 0.15$–0.25 that is not reproduced by the corresponding reduced-domain simulation. This feature lies adjacent to the inner buffer zone, where the temporal variability is largest, and a boundary origin cannot be excluded for either setup. Nevertheless, the reduced-domain setup captures the essential transport behavior while allowing us to systematically vary the local $E \times B$ shear.

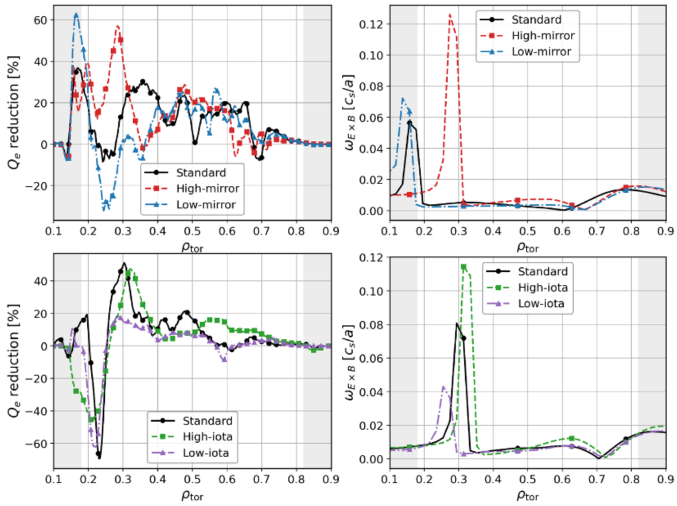

Figure 11. Percentage difference in electron heat flux ΔQ_e (*left column*) and the magnitude of the $E \times B$ shear rate $\omega_{E\times B}$ of equation (2), in units of c_s/a (*right column*). Grey shaded areas mark the buffer zones of the global simulations. *Top row*: mirror scan configurations. *Bottom row*: ι scan configurations. Positive ΔQ_e indicates suppression due to E_r, while negative values indicate destabilization.

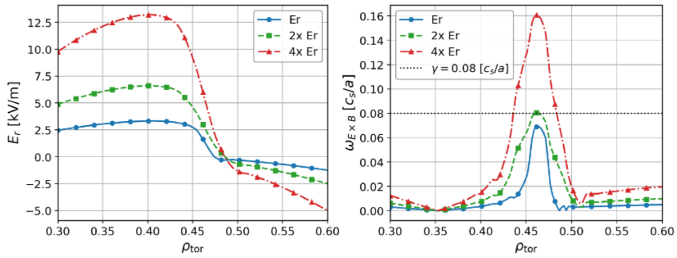

Figure 12. *Left*: imposed radial electric field E_r for the simulation centered at $\rho = 0.45$, with curves corresponding to the nominal profile (based on the high-mirror configuration) and approximately two and four times the nominal E_r amplitude. *Right*: corresponding $E \times B$ shear rate $\omega_{E\times B}$ (in units of c_s/a) for the three cases. The horizontal dotted line indicates the maximum linear growth rate $\gamma = 0.08\,c_s/a$ in the domain, obtained from a linear global simulation without a background E_r. Radial regions where $\omega_{E\times B} > \gamma$ are expected to be stabilized by shear decorrelation.

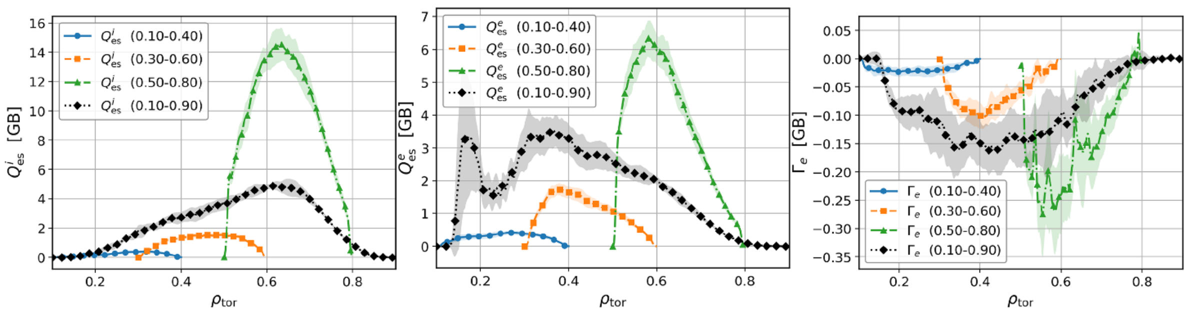

Figure 13. Comparison of ion heat flux (*left*), electron heat flux (*center*), and electron particle flux (*right*) obtained from the full radial domain (black) and from reduced domains centered at $\rho = 0.25$ (blue), 0.45 (orange), and 0.65 (green). All simulations shown are performed without an imposed background E_r.

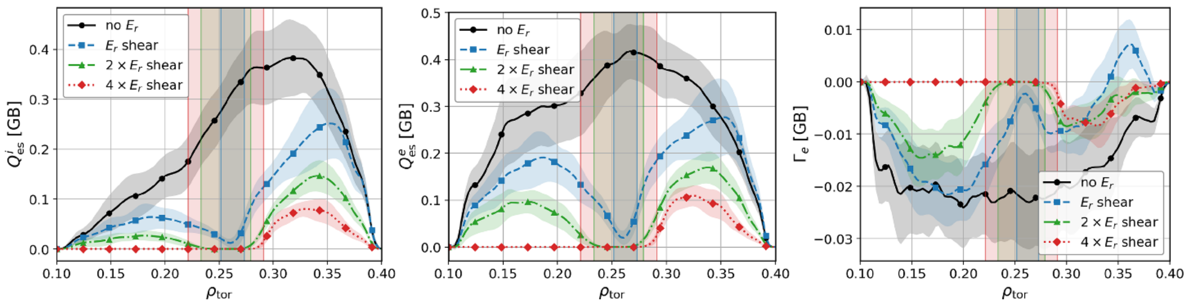

Figure 14. Ion heat flux (*left*), electron heat flux (*center*), and electron particle flux (*right*) for the reduced-domain simulation centered at $\rho = 0.25$. The shaded colored areas indicate the radial locations where the imposed $E \times B$ shear rate $\omega_{E\times B}$ equals the linear growth rate γ for the different E_r amplitudes. Inside these regions, the shear rate exceeds the linear growth rate, indicating where turbulent transport is expected to be suppressed.

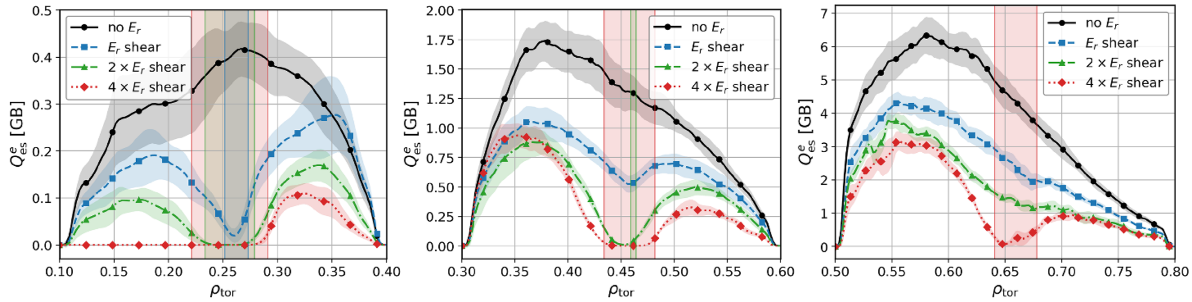

Figure 15. Electron heat flux for simulations centered at $\rho = 0.25$ (*left*), $\rho = 0.45$ (*center*), and $\rho = 0.65$ (*right*). The shaded colored areas indicate the radial locations where $\omega_{E\times B} = \gamma$. Increasing $E \times B$ shear progressively widens these regions and suppresses turbulent transport.

5.2. Transport response to $E \times B$ shear

We now analyze the response of turbulent transport to the imposed $E \times B$ shear. As a representative example, figure 14 shows the ion heat flux, electron heat flux, and electron particle flux for the simulation centered at $\rho = 0.25$. The curves correspond to the cases without imposed shear and with increasing E_r amplitudes (black—no shear, blue—nominal, green dash-dotted—$\sim 2 \times E_r$, and red dotted—$\sim 4 \times E_r$).

The shaded colored areas indicate the radial locations where the imposed $E \times B$ shear rate $\omega_{E\times B}$ equals the linear growth rate γ, obtained from linear global gyrokinetic simulations performed in each reduced domain without a background E_r. Inside these areas, $\omega_{E\times B} > \gamma$, while outside, the growth rate dominates. Since shear decorrelation is expected to suppress turbulence when the shear rate exceeds the growth rate [17–19], these regions provide an estimate of where turbulent transport stabilization is expected. The maximum growth rates for the domains centered at $\rho = 0.25$, 0.45, and 0.65 are $0.035\, c_s/a$, $0.08\, c_s/a$, and $0.14\, c_s/a$, respectively.

A clear correlation is observed between the predicted stabilization regions and the nonlinear transport levels. As the imposed shear increases, the radial region satisfying $\omega_{E\times B} > \gamma$ becomes wider, and turbulent transport is progressively reduced across a larger portion of the domain. In the strongest shear case, transport is strongly suppressed, reaching values close to zero over most of the simulation domain, indicating that shear decorrelation dominates the nonlinear saturation mechanism [17, 18]. Suppression is also observed in regions where $\gamma > \omega_{E\times B}$, i.e. where the classical shear decorrelation criterion is not formally met. This residual reduction reflects the globality of the simulated turbulence: modes have a finite radial extent and feel the strong shear from adjacent regions where $\omega_{E\times B} > \gamma$. The direct stabilizing effect of the background E_r [35, 36] can provide an additional contribution. In the strongest-shear case, the shear barrier also cuts off turbulence spreading from the strongly driven outer part of the domain. The region left inside it is bounded by the inner buffer zone on one side and by the region of $\omega_{E\times B} > \gamma$ on the other; given the weak local drive and the finite radial extent of the modes, turbulence is not self-sustained there, and the fluxes drop to negligible values.

We next compare how this effect depends on the radial position, which affects both the linear growth rate and the background transport drive. Figure 15 shows the electron heat flux for simulations centered at $\rho = 0.25$, 0.45, and 0.65; the ion heat flux and particle flux show qualitatively similar trends and are omitted here for clarity.

A clear radial dependence emerges from this comparison. The strongest stabilization occurs at $\rho = 0.25$, where two factors combine: the growth rate is smaller, resulting in lower intrinsic transport, and the radial region where $\gamma < \omega_{E\times B}$ is wider. At $\rho = 0.45$, the transport level is higher, and the region where $\gamma < \omega_{E\times B}$ narrows. For the nominal E_r case, there is essentially no radial region where the shear rate exceeds the growth rate, and the transport reduction is modest. Scaling E_r by $\sim 2\times$ and $\sim 4\times$ progressively enlarges the stabilized region, producing stronger transport suppression. At $\rho = 0.65$, only the $\sim 4 \times E_r$ case produces a region where $\gamma < \omega_{E\times B}$, with correspondingly stronger suppression, while the nominal and $\sim 2 \times E_r$ cases show only moderate reductions.

In conclusion, these results demonstrate that turbulent transport reduction is governed by the relationship between the imposed $E \times B$ shear and the linear growth rate [18, 19]. The effectiveness of shear suppression is largest where the growth rate is small and the radial extent of $\omega_{E\times B} > \gamma$ is wide. Conversely, regions with higher growth rates or limited shear-dominated areas exhibit only modest transport reduction. Overall, the nonlinear simulations are in quantitative agreement with the classical shear decorrelation criterion [17–19], confirming that increasing the imposed $E \times B$ shear systematically expands the stabilized regions and progressively suppresses turbulent transport.

6. Conclusions

We have presented a more detailed numerical analysis of the global GENE-3D simulations of [8], focusing on the turbulent transport channels and the role of the equilibrium radial electric field across mirror ratio and rotational transform (ι) configuration scans at fixed plasma profiles.

For the magnetic configuration scans, ion and electron heat fluxes show only mild sensitivity to both parameters, with the low-mirror configuration producing slightly higher heat fluxes. The particle flux exhibits a more pronounced dependence on the mirror ratio: the low-mirror configuration drives a strong inward density pinch mediated by passing electrons, while the high-mirror configuration shows a net outward flux [28]. For the ι scan, transport differences across configurations are small in the heat channels, with weaker fluctuations at higher ι in the deep core; the particle flux is more strongly inward in the low-ι configuration. The fluctuation trend agrees with the PCI measurements of [8], although the simulated differences are smaller in magnitude than those reported experimentally. For the mirror scan, the simulated density fluctuation levels do not reproduce the experimentally observed configuration dependence [8], as discussed in section 4. The same picture emerges from the synthetic PCI analysis [20]: the wavenumber and frequency spectra reproduce the experimental ordering reported in [8] for the ι scan, but show essentially no configuration dependence in the mirror scan at fixed profiles.

For the equilibrium radial electric field, the $E \times B$ shear significantly modifies electron heat transport in regions where it is strongest. The effect on ion heat flux is less pronounced, as the ion heat flux is already low in the region of strongest shear. A controlled parametric study confirms that suppression follows the classical shear decorrelation criterion [17–19]: it is strongest in the deep core, where growth rates are smallest and the shear-dominated region is widest, and weakens progressively toward the outer core, where only the strongest imposed E_r produces a region with $\omega_{E\times B} > \gamma$.

Since these simulations are performed at fixed plasma profiles that do not satisfy power balance, a direct quantitative comparison with the experimental observations is not straightforward. Coupling GENE-3D to TANGO [29–32] to evolve the profiles self-consistently is expected to modify the configuration-dependent trends, potentially bringing them closer to the experimental observations. This is supported by previous applications of the GENE–TANGO framework to W7-X discharges [33, 34], where self-consistent profile evolution was shown to bring simulations into quantitative agreement with experiment. Such coupled simulations are left for future work. The $E \times B$ shear was shown to significantly affect transport, particularly in the root-transition region, i.e. the radial region where the ambipolar radial electric field changes from the positive electron root to the negative ion root (section 5). A more careful modeling of this transition [37] should therefore be considered for future global simulations.

Acknowledgments

This work has been carried out within the framework of the EUROfusion Consortium, funded by the European Union via the Euratom Research and Training Programme (Grant Agreement No 101052200 — EUROfusion). Views and opinions expressed are however those of the author(s) only and do not necessarily reflect those of the European Union or the European Commission. Neither the European Union nor the European Commission can be held responsible for them. Furthermore, numerical simulations were performed on the Marconi Fusion supercomputer at CINECA, Italy.

Data availability statement

The data that support the findings of this study are available from the corresponding author upon reasonable request.

ORCID iDs

A. Bañón Navarro 0000-0003-0487-6395
L. Podavini 0000-0001-7872-3768
J.-P. Bähner 0000-0002-5828-2747
J. Smoniewski 0000-0002-4028-826X
S.K. Hansen 0000-0002-5146-1056
A. Di Siena 0000-0002-5430-6713
M. Porkolab 0000-0002-9518-4097
E.M. Edlund 0000-0001-5320-4996
A. von Stechow 0000-0003-0277-4600
S.A. Bozhenkov 0000-0003-4289-3532
O.P. Ford 0000-0002-5646-4758
G. Fuchert 0000-0002-6640-2139
A. Langenberg 0000-0002-2107-5488
N.A. Pablant 0000-0001-6617-8459
P.Zs. Pölöskei 0000-0001-7781-5599
T. Romba 0000-0002-2727-9385
A. Zocco 0000-0003-2617-3658
O. Grulke 0000-0001-7879-8671
F. Jenko 0000-0001-6686-1469

References

[1] Wolf R.C. *et al* 2017 *Nucl. Fusion* **57** 102020
[2] Beidler C.D. *et al* (the W7-X Team) 2021 *Nature* **596** 221
[3] Klinger T. *et al* 2019 *Nucl. Fusion* **59** 112004
[4] Ford O.P. *et al* (the W7-X Team) 2024 *Nucl. Fusion* **64** 086067
[5] Goodman A.G., Xanthopoulos P., Plunk G.G., Smith H., Nührenberg C., Beidler C.D., Henneberg S.A., Roberg-Clark G., Drevlak M. and Helander P. 2024 *PRX Energy* **3** 023010
[6] Guttenfelder W. *et al* 2025 *J. Plasma Phys.* **91** E83
[7] Lion J. *et al* 2025 *Fusion Eng. Des.* **214** 114868
[8] Bähner J.-P. *et al* (the W7-X Team) 2026 *Nucl. Fusion* **66** 016007
[9] Geiger J., Beidler C.D., Feng Y., Maaßberg H., Marushchenko N.B. and Turkin Y. 2015 *Plasma Phys. Control. Fusion* **57** 014004
[10] Xanthopoulos P., Mynick H.E., Helander P., Turkin Y., Plunk G.G., Jenko F., Görler T., Told D., Bird T. and Proll J.H.E. 2014 *Phys. Rev. Lett.* **113** 155001
[11] Bañón Navarro A., Merlo G., Plunk G.G., Xanthopoulos P., von Stechow A., Di Siena A., Maurer M., Hindenlang F., Wilms F. and Jenko F. 2020 *Plasma Phys. Control. Fusion* **62** 105005
[12] Stroteich S., Xanthopoulos P., Plunk G.G. and Schneider R. 2022 *J. Plasma Phys.* **88** 175880501
[13] Maurer M., Bañón Navarro A., Dannert T., Restelli M., Hindenlang F., Görler T., Told D., Jarema D., Merlo G. and Jenko F. 2020 *J. Comput. Phys.* **420** 109694
[14] Wilms F., Bañón Navarro A., Merlo G., Leppin L., Görler T., Dannert T., Hindenlang F. and Jenko F. 2021 *J. Plasma Phys.* **87** 905870604
[15] Helander P. 2014 *Rep. Prog. Phys.* **77** 087001
[16] Pablant N.A. *et al* (the W7-X Team) 2018 *Phys. Plasmas* **25** 022508
[17] Biglari H., Diamond P.H. and Terry P.W. 1990 *Phys. Fluids B* **2** 1
[18] Hahm T.S. and Burrell K.H. 1995 *Phys. Plasmas* **2** 1648
[19] Terry P.W. 2000 *Rev. Mod. Phys.* **72** 109
[20] Hansen S.K. *et al* 2022 *Plasma Phys. Control. Fusion* **64** 095011
[21] Turkin Y., Beidler C.D., Maaßberg H., Murakami S., Tribaldos V. and Wakasa A. 2011 *Phys. Plasmas* **18** 022505
[22] Jenko F., Dorland W., Kotschenreuther M. and Rogers B.N. 2000 *Phys. Plasmas* **7** 1904
[23] Beer M.A., Cowley S.C. and Hammett G.W. 1995 *Phys. Plasmas* **2** 2687
[24] Brizard A.J. and Hahm T.S. 2007 *Rev. Mod. Phys.* **79** 421
[25] Görler T., Lapillonne X., Brunner S., Dannert T., Jenko F., Merz F. and Told D. 2011 *J. Comput. Phys.* **230** 7053
[26] Hindenlang F.J., Plunk G.G. and Maj O. 2025 *Plasma Phys. Control. Fusion* **67** 045002
[27] Mantica P. *et al* 2009 *Phys. Rev. Lett.* **102** 175002
[28] Bañón Navarro A., Di Siena A., Jenko F., Merlo A. and Laude E. 2026 *Phys. Rev. E* **113** L043204
[29] Parker J.B., LoDestro L.L., Told D., Merlo G., Ricketson L.F., Campos A., Jenko F. and Hittinger J.A. 2018 *Nucl. Fusion* **58** 054004
[30] Di Siena A. *et al* (the ASDEX Upgrade Team and the EUROfusion MST1 Team) 2022 *Nucl. Fusion* **62** 106025
[31] Di Siena A., Bilato R., Bañón Navarro A., Bergmann M., Leppin L., Görler T., Poli E., Weiland M., Tardini G. and Jenko F. (the ASDEX Upgrade Team and the EUROfusion MST1 Team) 2024 *Nucl. Fusion* **64** 066020
[32] Di Siena A. *et al* (JET Contributors) 2025 *Nucl. Fusion* **65** 016050
[33] Bañón Navarro A., Di Siena A., Velasco J.L., Wilms F., Merlo G., Windisch T., LoDestro L.L., Parker J.B. and Jenko F. 2023 *Nucl. Fusion* **63** 054003
[34] Agapito Fernando D.L.C. *et al* (the W7-X Team) 2025 *Phys. Plasmas* **32** 073904
[35] Xanthopoulos P. *et al* (the W7-X Team) 2020 *Phys. Rev. Lett.* **125** 075001
[36] Sánchez E., Bañón Navarro A., Wilms F., Borchardt M., Kleiber R. and Jenko F. 2023 *Nucl. Fusion* **63** 046013
[37] Kuczyński M.D. *et al* 2025 *Nucl. Fusion* **65** 016019